Horizon 2020

Project title: AuTonomous intraLuminAl Surgery

State of the art of catheter shape sensing technology

Deliverable number: D2.2

Version 1.0.1

Funded by the European Union's Horizon 2020 research and innovation programme under the Marie Sklodowska-Curie Grant Agreement No. 813782

Project Acronym: ATLAS

Project Full Title: AuTonomous intraLuminAl Surgery

Call: H2020-MSCA-ITN-2018

Grant Number: 813782

Project URL: https://atlas-itn.eu

Deliverable nature:	Report (R)
Dissemination level:	file:///home/xuanthao/Desktop/Deliverable/Archive/chapters/Introduction.tex Public (PU)
Contractual Delivery Date:	October 1, 2019
Actual Delivery Date	October 14, 2019
Number of pages:	26
Keywords:	SOA, Literature review, value analysis
Authors:	HA Xuan Thao, KU Leuven Sujit Kumar Sahu, SSSA
Peer review:	Emmanuel Vander Poorten, KU Leuven

Abstract

Flexible devices are increasingly being used to diagnose or intervene in the hospital. Their inherent compliancy provides them the ability to conform to complex environments and navigate through tortuous, often fragile, environments. As flexible devices bend away upon contact, their overall shape is determined through a complex interplay between amongst others steering commands, anatomy and physiological parameters. Expert surgeons rely on profound knowledge of the anatomy and a lot of experience when judging how a flexible device is positioned inside the human body. But even then they stand generally positive towards technology that could give them a better insight in the actual, distributed spatial configuration of these flexible instruments. To meet with these requests various 'shape sensing' techniques have been developed over the past decade. While these techniques have not yet reached adoption in a clinical setting, a breakthrough in the coming years is expected. This deliverable provides a concise overview of the different techniques that have been presented throughout the literature. The survey focuses mainly on catheter applications, but one can imagine that similar technology could be embedded in other flexible devices such as flexible scopes, colonoscopes or - depending on the size - on flexible needles. Furthermore, shape sensing technology is considered a crucial technology for developing autonomous steering technology for flexible instruments, which forms the topic of study of the Marie-Curie Training Network *ATLAS*.

Contents

List of Figures

List of Tables

1 Introduction

Intraluminal navigation is a particularly sophisticated procedure which forms a part in many Minimally Invasive Surgical (MIS) interventions. The task concerns steering flexible instruments such as catheters or endoscopes through fragile body lumens as there are the colon, the ureter, esophagus, trachea, bronchi or vessels from the cardiovasculature system. This type of tasks take advantage of the compliant nature of these flexible instruments which allows them to reach deeply seeted treatment sites with complex morphologies or that are only accessibly through tortuous and highly constrained access routes. Flexible instruments are usually navigated manually by the operator. Due to advances in actuation and sensing technologies, recently robot-assisted MIS has grown in popularity. The *ATLAS* project, which stands for "AuTonomous inTraLuminAl Surgery" is a Marie Training Network. This is a European Joint Doctorate School targeting the training of experts in a very specific branch of robotic surgery. *ATLAS* will develop smart flexible robots that can autonomously drive though complex deformable tubular structures. There exist ample clinical applications that can benefit from autonomous flexible robots such as colonoscopy, colorectal surgery or cardiovascular procedures. To achieve precise and reliable motion control of these distributed systems, the spatial information of the robot needs to be acquired such that it can be used e.g. in a feedback loop by a robot controller. Not only that, in an earlier stage, the gained spatial information could already help clinicians understand how to handle these flexible devices more adequately during manual operation.

Currently, surgeons rely on haptic feedback, adjusting their steering commands based on the resistance they feel. However, the interaction force is masked by friction along the lumen wall or friction in the trocar or access port. Overall this way of steering is not very precise and can cause overly large stresses applied on already fragile tissue. Sometimes, ultrasound or fluoroscopy are used to give information about the shape and position of the flexible instruments during interventions. However, these methods have some important disadvantages. Fluoroscopy is harmful for the patient, it offers limited contrast, spatial resolution is poor and only 2-dimensional. Further, contrast agents that may be injected to enhance optical contrast can cause nephrotoxicity. Ultrasound may only show a small part of the scene (e.g. forward- or side-ways looking ultrasound provides no information on the tail of the instrument) and can be quite noisy, under influence of shadows or speckles. The need for methods that can accurately estimate the entire shape of the catheters and by extension flexible instruments in 3D and in real-time is high. Modeling alone, e.g. based on pre-operative data, kinematic and constitutive instrument models has its limitations. This is because the environment is dynamic and deformable and the contacts are distributed and inherently hard to model and predict. A combination with intra-operative sensing is a pre-requisite. Where MRI and fluoroscopy may be available, these sensing techniques are or damaging or have only poor spatial or temporal resolution. They cannot be employed stand-alone for real-time distributed estimation. This report therefore focuses, aside from imaging, mainly on proprioceptive sensing methods. These are sensors that are embedded in the flexible instrument bodies themselves and are targeted to estimate the shape and pose from within. The report discusses the mechanism, pros and cons of different sensor methods for shape reconstruction of flexible instruments. Figure 1.1 provides a schematic overview of the different categories that have been identified and that will be elaborated upon in the remainder of this deliverable.

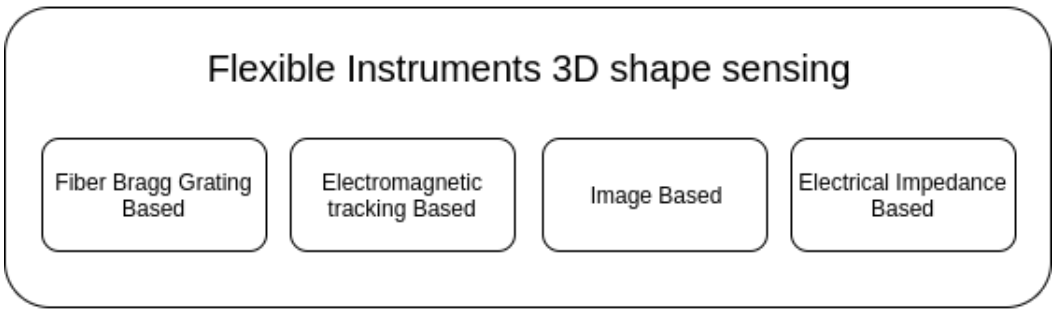

Figure 1.1: Main categories of sensing methods to estimate 3D shape of flexible instruments.

2 Fiber Bragg Grating based shape sensing

Optical sensors are now increasingly used in numerous medical applications. Their small size, light weight and high elasticity allow easy integration and miniature designs with low effects on the overall stiffness of the flexible instrument. Moreover, their immunity to electromagnetic interference, compatibility with governing medical imaging modalities [51] make optical fibers very well suitable for medical applications. For shape sensing with Fiber Bragg Grating (FBG) form the most common class of sensors. FBG sensors have been applied to reconstruct the 3D shape of continuum manipulators [46] or to monitor the deflection of needles e.g. used during MRI-Guided intervention [33]. An FBG sensor is obtained by illuminating a regular pattern of an optical fiber with a laser, which modifies the refractional index of that part that is illuminated. Each FBG sensor will then reflect a narrow band of spectrum of incoming light (the wavelength being determined by the distance between the illuminated regions). The wavelengths belonging to other ranges are lossless transmitted. When multiple gratings are used, typically each will have their own central wavelength. The gratings are fabricated in such manner that each central wavelength is separated sufficiently far from the other. The reflected light from one grating can therefore be distinguished easily from the light reflected by the other gratings. The reflected spectrum of one grating changes due to the temperature variations, mechanical strain or torsion applied on the optical fiber. By measuring the central wavelength shift of the reflected light, by an interrogator connected to the optical fiber, the instantaneous temperature, curvature or force can be estimated. Shape reconstruction based on FBGs relies on curvature and torsion estimates at the discrete locations where the gratings are inscribed[1]. An interpolation process is then carried out to calculate the curvature and torsion in between the gratings. Finally, the entire shape is then reconstructed using a space curve shape reconstruction method.

1 Strain computation

The strain on each fiber can be computed as follows at the discrete locations of the FBG sensors. The wavelength at which the reflection is highest is referred to as the Bragg wavelength $\lambda_B \in \mathbb{R} > 0$ of the FBG. When there is a change in strain or in temperature, the Bragg wavelenth will shift by an amount of $\Delta\lambda_B$. The relationship between experienced strain and temperature is shown as [12]:

$$\frac{\Delta\lambda_B}{\lambda_B} = (1 - p_e)\varepsilon + (\alpha_\Lambda + \alpha_n)\Delta T, \tag{2.1}$$

where p_e is a constant parameter that captures the contribution of the photoelastic effect[2], α_Λ and α_n are the thermal expansion[3] and thermal-optic coefficient[4], respectively. Symbol ε represents the applied strain and ΔT is the change in temperature. In case of constant temperature, (3.8) simplies to:

$$\frac{\Delta\lambda_B}{\lambda_B} = (1 - p_e)\varepsilon. \tag{2.2}$$

2 Curvature and bending angle computation

The relationship between the axial strain in the optical fiber, the distance (r) of the fiber to the neutral axis and the curvature of the fiber is [9]

$$\varepsilon = -\frac{r}{p} = -\kappa r \tag{2.3}$$

where p is the radius of curvature and κ is the curvature. Using (2.2) and (2.3), the curvature of the optical fiber can now be derived by measuring the wavelength shift.

For recontstructing a full 3D-curve a single optical fiber or a single core with gratings does not suffice. Instead multiple fibers or in the case of a multi-core fiber, multiple parallel cores are needed. These fibers or cores are commonly arranged

[1] Without loss of generalisation, the location where a grating is inscribed will be referred in the following as 'the FBG sensor'.
[2] The refraction index itself changes when undergoing axial stress. This effect is captured by the photoelastic parameter p_e.
[3] The thermal expansion coefficient capture the change in strain of the fiber as function of variations in temperature.
[4] The thermal-optic coefficient relates how the refraction index changes as function of the temperature.

in an orthogonal or a triangular configuration. In extended position, a flexible instrument, will embed three straight optical fiber for the triangular configuration or four optical fibers in the orthogonal configuration. For both an additional fiber may be arranged in the center of the triangle or of the square. Through this configuration it becomes possible to measure curvature and change in bending plane. RJ Roesthuis *et al.* designed a flexible nitinol needle which composes three equally spaced optical fibers in [41]. Multiple FBG sensors are distributed along the optical fibers to estimate the bending curvature at discrete values of the arc length. These discrete values enable the reconstruction of the 3D needle shape. The relationship between the axial strain for a needle in pure bending and the distance from the neutral axis is given in (2.3). Thus, for an arrangement of three parallel FBGs, the set of following equations can be derived for the strain at the location of the different fibers (denoted by a, b and c) at a cross section (typically through the centre of the gratings) of the needle:

$$\begin{aligned} \varepsilon_a &= -\kappa r_a \sin(\varphi) + \varepsilon_0 \\ \varepsilon_b &= -\kappa r_b \sin(\varphi + \gamma_b) + \varepsilon_0. \\ \varepsilon_c &= -\kappa r_c \sin(\varphi + \gamma_b + \gamma_c) + \varepsilon_0 \end{aligned} \tag{2.4}$$

Assume, without loss of generality, that a coordinate frame is attached rigidly to the cross-section with an y-axis pointing from the center of the cross-section (at the intersection with the neutral line), through the first fiber a (which is at distance r_a to the origin) and that γ is the angle that indicates the direction of curvature. The bias ε_0 is assumed to be equal for each FBG. It is caused by the change in temperature or external forces acting on the needle during strain measurements. The distance from the neutral axis to the FBG sensor (r_a, r_b and r_c) and the angles $\gamma_a = 0, \gamma_b$ and γ_c are known and constant. The set of equations (2.4) can then be used to solve for unknown parameters (needle curvature κ, direction of curvature φ and the bias ε_0) in closed form.

Jason P. Moore *et al.* suggested another method to calculate the bending direction and radius of curvature in case of symmetrically arranged tricore fibers [27]. Large curvature errors can be caused by strain measurement error. To calculate the curvature using information from all cores and reduce the effect of strain measurement errors, the apparent curvature vector which points in the direction of the i^{th} from the center of the optical fiber is defined as below:

$$\kappa_{app,i} = -\frac{\varepsilon_i}{r_i}(\cos(\gamma_i)j + \sin(\gamma_i)k), \tag{2.5}$$

where j and k are unit vectors that are aligned with the local y and z axes. For N number of cores in the fiber, the vector sum of the apparent curvature vectors is

$$\kappa_{app,i} = -\sum_{i=1}^{N} \frac{\varepsilon_i}{r_i} \cos(\gamma_i)j + \sum_{i=1}^{N} \frac{\varepsilon_i}{r_i} \sin(\gamma_i)k. \tag{2.6}$$

In the symmetric case, the distance from the center of the fiber to each core can be approximated to be the same r, the curvature κ and local bending direction φ can be determined as below:

$$\kappa = \frac{2|\kappa_{app}|}{N} = \frac{\sqrt{(\sum_{i=1}^{N} \frac{\varepsilon_i}{r_i} \cos(\gamma_i))^2 + (\sum_{i=1}^{N} \frac{\varepsilon_i}{r_i} \sin(\gamma_i))^2}}{Nr} \tag{2.7}$$

$$\varphi = angle(\kappa_{app}) \tag{2.8}$$

3 Curvature and bending angle interpolation

The discrete value of the curvature and the bend direction ϕ are calculated. The intermediate curvatures and direction angles are determined by e.g. a linear or cubic interpolation. Henken *et al.* compared different interpolation methods and concluded that cubic spline interpolation is superior [11]. Moreover, the measurements of one FBG array are normally the values for one specific location which is the array center. Sonja Jäckle *et al.* proposed a novel approach which takes the FBG geometry into account for the curvature interpolation by modeling the measured value as an average over the sensor range [16]. Interpolating the intermediate curvature and bend direction is the most popular approach. However, Sonja Jäckle *et al.* showed in [17] that especially interpolating the bend direction interpolation is not straightforward for flexible structure because of discontinuouties in the angle. They confirmed experimentally that interpolating the bending angle leads to overshoots before and after the discontinuity. Interpolating of the strain results in better accuracy for bend angle and the curvature is close to zero at discontinuity point. Thus, they recommended to interpolate the strain before

calculating the curvature and bend angle since it results in more realistic curvatures and bend angles. Overall this then leads to a more accurate shape estimation.

4 Space curve shape reconstruction

The shape of flexible instruments is normally modeled as a space curve. The shape of such space curve is defined by two intrinsic quantities: the curvature and the torsion. The curvature is the rate of change of the tangential direction caused by the bending of the instrument. The torsion is the rate of change of the bending direction. The relationship between the space curve and these two quantities is captured e.g. by the Frenet-Serret formulas:

$$\begin{aligned} \frac{d\hat{t}(s)}{ds} &= \kappa(s)\hat{n}(s) \\ \frac{d\hat{n}(s)}{ds} &= -\kappa(s)\hat{t}(s) + \tau(s)\hat{b}(s) \\ \frac{d\hat{b}(s)}{ds} &= -\tau(s)\hat{n}(s) \end{aligned} \tag{2.9}$$

where τ denotes the torsion, and $\hat{t}, \hat{n}$ and $\hat{b}$ denote the tangent, normal and binormal vectors, respectively. The arc length (or lenght over the curve neutral axis) is here denoted as s. The TNB frame or Frenet-Serret frame at a point with arc length s on the 3D space curve $C(s)$ is defined as follows:

$$\begin{aligned} \hat{t}(s) &= \frac{C'(s)}{||C'(s)||} \\ \hat{n}(s) &= \frac{\hat{t}'(s)}{||\hat{t}'(s)||} \\ \hat{b}(s) &= \hat{t}(s) \times \hat{n}(s) \end{aligned} \tag{2.10}$$

The curvature κ and torsion τ can be calculated from the above relation as

$$\begin{aligned} \kappa(s) &= ||\hat{t}'(s)|| \\ \tau(s) &= -\frac{\hat{b}'(s)}{\hat{n}(s)} \end{aligned} \tag{2.11}$$

In the case of a limited number of FBG-sensors, the curvature and torsion are not given as continuous functions. They are given as a finite number of values at equally spaced nodes on the curve. The space curve $C(s)$ is thus divided into a finite number, N_s, of equal length segments. The length of each segment is $\Delta s = \frac{L}{N_s}$, where L is the total length of the sensorized part of the space curve. Let $C_k = C(k\Delta s), \hat{t}_k = \hat{t}(k\Delta s), \hat{n}_k = \hat{n}(k\Delta s)$ and $\hat{b}_k = \hat{b}(k\Delta S)$. The problem is now restated as: given the curvature κ_k and torsion τ_k for each segment, find the position of n^{th} nodes, C_n, where $1 \leq n \leq N_s$ from the known initial condition $C_0, \hat{t}_0, \hat{n}_0$ and $\hat{b}_0$. Sungyeop Lim *et al.* used various numerical methods to solve the system of ODEs to reconstruct the shape of the space curve [22] including: the Euler method, the 4th order Runge-Kutta method and the helical extension method (HEM). The shape of the 3D space curve is reconstructed from its curvature and torsion by repetitive updating the TNB frame as follow:

$$\begin{aligned} \hat{t}_{k+1} &= \hat{t}_k + \int_{k\Delta s}^{(k+1)\Delta s} \kappa(\sigma)\hat{n}(\sigma)d\sigma \\ \hat{n}_{k+1} = \hat{n}_k - \int_{k\Delta s}^{(k+1)\Delta s} \kappa(\sigma)\hat{t}(\sigma)d\sigma &+ \int_{k\Delta s}^{(k+1)\Delta s} \tau(\sigma)\hat{b}(\sigma)d\sigma \\ \hat{b}_{k+1} &= \hat{b}_k - \int_{k\Delta s}^{(k+1)\Delta s} \tau(\sigma)\hat{n}(\sigma)d\sigma \end{aligned} \tag{2.12}$$

To each segment numerical values of curvature and torsion are assigned rather than the continuous functions. To simplify the analysis, the curvature and torsion are assumed to be constant within a segment. To solve the problem using the Euler

method, the TNB frames are updated as below:

$$\begin{aligned} \hat{t}_{k+1} &= \hat{t}_k + \kappa_k \Delta s \hat{n}_k \\ \hat{n}_{k+1} &= \hat{n}_k - \kappa_k \Delta s \hat{t}_k + \tau_k \Delta s \hat{b}_k \\ \hat{b}_{k+1} &= \hat{b}_k - \tau_k \Delta s \hat{n}_k \end{aligned} \tag{2.13}$$

By assuming the curvature and torsion constant within a segment, the orthonormality of the TNB frame is lost because all $\hat{t}_{k+1}.\hat{n}_{k+1}, \hat{n}_{k+1}.\hat{b}_{k+1}$ and $\hat{b}_{k+1}.\hat{t}_{k+1}$ cannot be zero unless either one of the curvature or torsion is zero. Another point to notice is that the magnitudes of $\hat{t}_{k+1}, \hat{n}_{k+1}$ and $\hat{b}_{k+1}$ are not 1. Thus, a compensation algorithm need to be applied to make up for the orthonormality loss while using the Euler method. One can use the method mentioned in [22].

$$\begin{aligned} \hat{t}^{rect}_{k+1} &= \frac{\hat{t}_{k+1}}{|\hat{t}_{k+1}|} \\ \hat{n}^{rect}_{k+1} &= \frac{\hat{b}_{k+1} \times \hat{t}^{rect}_{k+1}}{|\hat{b}_{k+1} \times \hat{t}^{rect}_{k+1}|} \\ \hat{b}^{rect}_{k+1} &= \hat{t}^{rect}_{k+1} \times \hat{n}^{rect}_{k+1} \end{aligned} \tag{2.14}$$

This compensation algorithm can help re-orthonormale the TNB frame and keep the method functioning. However, there is also the chance that the result deviates even further from the true value of $\hat{t}_{k+1}, \hat{n}_{k+1}$ and $\hat{b}_{k+1}$ by this compensation process. Another solution to solve for the TNB frame is to use higher-order methods such as the 4th order Runge-Kutta mehod. The TNB frame is now updated as follows:

$$\begin{aligned} \hat{t}_{k+1} &= \hat{t}_k + \frac{\Delta s}{6}(a_{t1} + 2a_{t2} + 2a_{t3} + a_{t4}) \\ \hat{n}_{k+1} &= \hat{n}_k + \frac{\Delta s}{6}(a_{n1} + 2a_{n2} + 2a_{n3} + a_{n4}) \\ \hat{b}_{k+1} &= \hat{b}_k + \frac{\Delta s}{6}(a_{b1} + 2a_{b2} + 2a_{b3} + a_{b4}) \end{aligned} \tag{2.15}$$

where

$$\begin{aligned} a_{t1} &= \kappa_k \hat{n}_k \\ a_{n1} &= -\kappa_k \hat{t}_k + \tau_k \hat{b}_k \\ a_{b1} &= -\tau_k \hat{n}_k \\ a_{t2} &= \kappa_k \left(\hat{n}_k + \frac{\Delta s}{2} a_{n1} \right) \\ a_{n2} &= -\kappa_k \left(\hat{t}_k + \frac{\Delta s}{2} a_{t1} \right) + \tau_k \left(\hat{b}_k + \frac{\Delta s}{2} a_{b1} \right) \\ a_{b2} &= -\tau_k \left(\hat{n}_k + \frac{\Delta s}{2} a_{n1} \right) \\ a_{t3} &= \kappa_k \left(\hat{n}_k + \frac{\Delta s}{2} a_{n2} \right) \\ a_{n3} &= -\kappa_k \left(\hat{t}_k + \frac{\Delta s}{2} a_{t2} \right) + \tau_k \left(\hat{b}_k + \frac{\Delta s}{2} a_{b2} \right) \\ a_{b3} &= -\tau_k \left(\hat{n}_k + \frac{\Delta s}{2} a_{n2} \right) \\ a_{t4} &= \kappa_k (\hat{n}_k + \Delta s a_{n3}) \\ a_{n4} &= -\kappa_k (\hat{t}_k + \Delta s a_{t3}) + \tau_k (\hat{b}_k + \Delta s a_{b3}) \\ a_{b4} &= -\tau_k (\hat{n}_k + \Delta s a_{n3}) \end{aligned} \tag{2.16}$$

However, the truncation error cannot be completely eliminated by using conventional numerical methods even with higher order methods. Also the problem of orthonormality still remains. Therefore, the use of the compensation algorithm (2.14) is necessary. In short, numerical methods are not recommended. In case high precision is needed, the HEM method,

discussed further, is recommended. The position of each node that belongs to the space curve can be calculated from the definition of the tangent vector:

$$C(s) = \int_0^s \hat{t}(\sigma)d\sigma \tag{2.17}$$

An approximation of C_{k+1} can be calculated by the trapezoidal rule as follow:

$$C_{k+1} = C_k + \frac{\Delta s}{2}(\hat{t}_k + \hat{t}_{k+1}) \tag{2.18}$$

In [22], the authors proposed a novel approach called HEM to reconstruct the shape of a space curve by treating each segment as a segment of a helix. Using a given torsion and curvature of a segment, a helix that approximates the form of this segment is found. For a helix coiled around the z-axis with radius R, verical elevational H and rotational rate Ω, the parametric equation in terms of the arclength parameter s can be written as [21]:

$$C(s) = \begin{bmatrix} R\cos\Omega s \\ R\sin\Omega s \\ Hs \end{bmatrix} \tag{2.19}$$

In case $C(s)$ is a unit-speed curve, the following condition holds:

$$\left\| \frac{dC(s)}{ds} \right\| = \sqrt{R^2\Omega^2 + H^2} = 1 \tag{2.20}$$

From (2.10), the TNB frame can be calculated as

$$\hat{t}(s) = \begin{bmatrix} -R\Omega\sin\Omega s \\ R\Omega\cos\Omega s \\ H \end{bmatrix} \tag{2.21}$$

$$\hat{b}(s) = \begin{bmatrix} -\cos\Omega s \\ -\sin\Omega s \\ 0 \end{bmatrix} \tag{2.22}$$

$$\hat{n}(s) = \begin{bmatrix} H\sin\Omega s \\ -H\cos\Omega s \\ R\Omega \end{bmatrix} \tag{2.23}$$

R, H and Ω can be determined from its κ and τ as:

$$\begin{aligned} R &= \frac{\kappa}{\kappa^2 + \tau^2} \\ H &= \frac{\tau}{\sqrt{\kappa^2 + \tau^2}} \\ \Omega &= \sqrt{\kappa^2 + \tau^2} \end{aligned} \tag{2.24}$$

In HEM, the TNB frame is updated by rotating the three vectors by the angle of $\gamma = \Omega\Delta s$ about vector $\hat{w}$. According to Rodrigues' formula [1], the vector v_{rot} that is obtained by rotating a vector v about an axis $\hat{w} = [w_1\ w_2\ w_3]^T$ by an angle γ is given as:

$$v_{rot} = \cos\gamma v + \sin\gamma(\hat{w} \times v) + (1 - \cos\gamma)(\hat{w}.v)\hat{w} = Rv, \tag{2.25}$$

where the rotation matrix R can be written as:

$$R(s) = \begin{bmatrix} X + w_1^2(1-X) & w_1w_2(1-X) - w_3Y & w_3w_1(1-X) + w_2Y \\ w_1w_2(1-X) + w_3Y & X + w_2^2(1-X) & w_2w_3(1-X) - w_1Y \\ w_3w_1(1-X) - w_2Y & w_2w_3(1-X) + w_1Y & X + w_3^2(1-X) \end{bmatrix} \tag{2.26}$$

where $X = \cos\gamma$ and $Y = \sin\gamma$. The TNB frame can be updated as

$$\begin{aligned} \hat{t}_{k+1} &= R\hat{t}_k \\ \hat{n}_{k+1} &= R\hat{n}_k \\ \hat{b}_{k+1} &= R\hat{b}_k \end{aligned} \tag{2.27}$$

Finally, the node positions are calculated as:

$$C_{k+1} = C_k + R\hat{n} + H\Delta s\hat{w} - R\hat{n}_{k+1} \tag{2.28}$$

To compare the performance of the Euler, 4th order Runge-Kutta and HEM method, the Jinguer space curve of length $L = 1000$ is defined and divided into N_seg segments to check the convergence of algorithm in [22]. The node positions are computed by two methods - 4th order Runge-Kutta and HEM then the error of node positions are observed. There were significant improvements in accuracy with the use of HEM. The error was reduced by 6.9-74.6% for $N_seg = 25$ and 8.6-92.7% for $N_seg = 100$. RJ Roesthuis *et al.* used another approach to estimate the shape of the needle during insertion in [41]. By attaching an appropriate local coordinate frame to the beginning of each segment, the shape can be reconstructed. It was reported in the paper that large discrepencies was observed between the reconstructed needle shape and deflection measured using camera images when there are complex bends i.e., out-of-plane bending cases. HEM is considered a better approach to reconstruct the space curve compared to the method reported in [41].

5 Discussion

Beside the triplet design with a triangular configuration, Sungyeop Lim *et al.* proposed the use of FBG sensors in triple-helix configuration to measure the bending and twist deformation simultaneously in [23]. They reported that the method can estimate the shape of a deformed cylinder with remarkable precision. Shape sensing techniques based on FBGs mainly rely on curvature estimated from the strain calculated from the wavelength shift. However, these techniques have been mostly applied for continuum robots under small deformation such as steerable interventional needdles for biospy or ablation applications because they have inherent properties of high stiffness to support the nearly perfect strain transfer to the attached FBG sensors. Unfortunately, when considering other instruments such as catheters, the majority of these have rather low stiffness which results in lower strain transfer efficiency onto the FBG sensors. Shahriar Sefati *et al.* showed that many geometric assumptions regarding the sensor design and the limited number of sensing locations make that conventional model-dependent FBG based position estimation is prone to significant error propagation that become especially apparent when the flexible instruments undergo large deflections [47]. Sefati *et al.* proposed a new approach based on a regression model that takes the FBG wavelength as the input and estimates the tip's position of the continuum robot. After the experiments, they concluded that the this data-driven method outperformed conventional model-dependent method. However, in this work, the data-driven method is used only to estimate the position of the tip of the continuum robot. Further investigation is needed to expand this method to reconstruct the complete shape of the robot. Moreover, the experiment was carried out in case there wasn't any contact between the continuum robot and the surrounding environment which means that a huge data-set and more complex model would be needed to cover all these cases. Seok C.R *et al.* proposed composite tubular shape sensor which provides sufficient torsional rigidity and flexural compliance through the use of wire braid reinforcement in [42]. A spacious tool channel can also be acquired with this design. They derived a mechanics-based model which includes an interfacial shear model and a fiber reinforcement model to identify the important design variables. This model is then validated through simulation and experiment. The lengthy structures and complex bending of the catheters require employing multiple FBGs to provide sufficient curvature information. Further investigation should be made to improve shape estimation of lengthy, low stiffness structures that undergo large deformations such as steerable catheters or endoscopes.

Note that once the shape has been computed different relevant analysis can be conducted. For example Qiao *et al.* determined the location and the amplitude of external forces that act along the length of a flexible body by analysing the

shape of that flexible body [34]. The quality of such *force-from-shape* analysis clearly depends on the quality of the shape estimate as well as on the level of deformation of the body.

3 Electromagnetic tracking based shape sensing

Electromagnetic (EM) tracking systems allow localizing small sensors inside the magnetic field. Physically, EM tracking uses magnetic field of known geometry created by a field generator to determine the pose of sensors by measuring magnetic flux or magnetic field. Typically not the absolute value, but the gradient is measured [8]. EM tracking based shape sensing is a shape reconstruction method which relies on determining the location and orientation of multiple EM sensors attached along the flexible instruments. There is no prior curvature information needed. Fewer sensors are used compared to FBG based shape sensing method as overall the sensors are larger and more difficult to integrate. The problem of line-of-sight is solved which enables to track and localize the flexible instruments within the human body. The small size of EM sensors allow them to be employed in different medical instruments without changing their mechanical properties too dramatically. The workspace over which the sensors can be tracked may be limiting. Also this type of sensors is easily disturbed if magnetic or ferromagnetic material is introduced in the workspace. Compared to FBG an advantage is that the absolute pose and orientantion can be estimated relative to an external world reference coordinate frame.

1 Shape reconstruction

To track the distal tip and the shape of flexible instruments, multiple miniature EM sensors can be attached along the instruments. The disadvantage of EM sensors is that they only provide the discrete position and orientation (typically 5 or 6 DoF). To overcome this disadvantage, S. Song *et al.* [49] proposed a method to reconstruct the shape of a continuum robots based on the positional and directional information from the distributed EM sensors and the curve length information. The shape reconstruction is done by fitting multiple quadratic Bézier curves. This is a general shape reconstruction method for flexible robots or concentric tube robots with multiple bending section. There are only $\lceil N/2 \rceil$ EM sensors needed to reconstruct the shape of an N-section robot. The EM sensors are mounted at the tail of the $(N-2k)^{th}$ section, where $0 \leq k \leq n/2$. A Bézier curve is a parametric curve that uses the Bernstein polynomials as a basis. A Bézier curve of degree n is represented by

$$B(t) = \sum_{t=0}^{n} b_{i,n}(t) P_i \tag{3.1}$$

where $0 \leq t \leq 1$. P_0 is the start point, P_n is the end point and $P_i (0 < i < n)$ are the control points. All the Bézier points and the basis function $b_{i,n}(t)$ determine the shape of the curve. The basis function $b_{i,n}(t)$ is defined as below:

$$b_{i,n} = \binom{n}{i} t^i (1-t)^{(n-i)} \tag{3.2}$$

In [49], the Song *et al.* proposed to model each section of the continuum robot as a quadratic Bézier curve. Assume that the continuum robot contains N sections, the k-section will be modeled by the start point P_{2k-2}, the end point P_{2k} and the control point P_{2k-1}. The explicit point form of the k-section is in this case:

$$B(t) = (1-t)^2 P_{2k-2} + 2(1-t)t P_{2k-1} + t^2 P_{2k} \tag{3.3}$$

where $0 \leq t \leq 1, 1 \leq k \leq N$.

The EM sensors are attached on the tail of the $(N-2k)^{th}$ section. In other word, the sensors will be mounted at position $P_{2(N-2k)}$. To start the shape reconstruction process, the continuum robot is devided into $\lceil N/2 \rceil$ groups. If the number of sections is even, each group contains two sections. The parameters of two quadratic Bézier curves will be figured out by information captured from two EM sensors (one is mounted at the starting point of the first section and the other sensor is mounted at the end point of the second section). In general, for the group containing k-th section and $(k+1)$-th section, the EM sensors are mounted at P_{2k-2} and P_{2k+2}. The known parameters from two sensors are positions of point P_{2k-2}, P_{2k+2} and tangent vectors of these two points H_{2k-2}, H_{2k+2}, respectively. Combining with the given information about the curve length of each section L_k and L_{k+1}, we need to solve for $S_{2k-2,2k-1}$ and $S_{2k+1,2k+2}$. The relationships

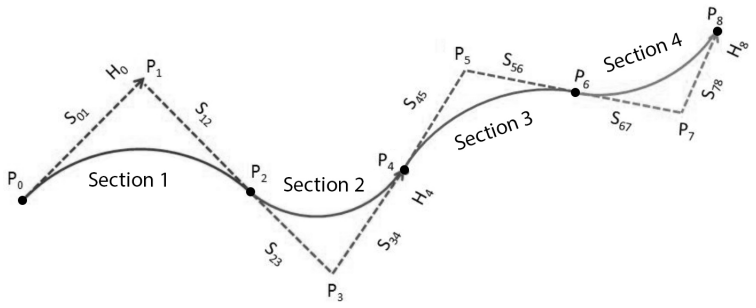

Figure 3.1: A four sections continuum robot is approximated by four quadratic Bézier curves. Two EM sensors are mounted on the robot. One is attached at the tail of second section (P_4) and the other is at the tail of the fourth section (P_8).

between these parameter are given below:

$$\begin{aligned} P_{2k-1} &= P_{2k-2} + S_{2k-2,2k-1}H_{2k-2} \\ P_{2k+1} &= P_{2k+2} - S_{2k+1,2k+1}H_{2k+2} \\ P_{2k} &= P_{2k-1} + Sk(P_{2k+1} - P_{2k-1}) \end{aligned} \tag{3.4}$$

where

$$Sk = \frac{S_{2k-2,2k-1}}{S_{2k-2.2k-1} + S_{2k+1,2k+2}}.$$

The equations of the two Bézier curves are defined as:

$$\begin{aligned} B_k(t) &= (1-t)^2P_{2k-2} + 2(1-t)tP_{2k-1} + t^2P_{2k} \\ B_{k+1}(t) &= (1-t)^2P_{2k} + 2(1-t)tP_{2k+1} + t^2P_{2k+2} \end{aligned} \tag{3.5}$$

Together with the section length information L_k and L_{k+1}, $S_{2k-2,2k-1}$ and $S_{2k+1,2k+2}$ can then be solved.

$$\begin{aligned} L_k &= L_{sk} \\ L_{k+1} &= L_{s(k+1)} \end{aligned} \tag{3.6}$$

where

$$L_{sk} = \sum_{i=1}^{n_k} \left\| B_k\left(\frac{i}{n_k}\right) - B_k\left(\frac{i-1}{n_k}\right) \right\|$$

where n_k is the number of points that are used to estimate the curve length for k-th Bézier curve.

In case there is an odd number of sections, the first group will contain one section and will be modeled as one Bézier curve. The first sensor will be mounted at P_2. The known parameters are P_0, H_0, P_2 and the curve length L_1. The missing parameter to define the Bézier curve for the first section is P_1. As one can see from Fig.3.1, $P_1 = P_0 + S_{01}H_0$, where $S_{01} = \|P_0P_1\|$. The length of each segment L_1 is equal to the length of curve B_1. Thus, we need to solve for S_{01}. The equation for solving the parameter is

$$L_1 - L_{s1} = 0 \tag{3.7}$$

where

$$L_{s1} = \sum_{i=1}^{n} \left\| B_1\left(\frac{i}{n}\right) - B_1\left(\frac{i-1}{n}\right) \right\|.$$

The explicit form of the Bézier curve for the first section is shown below:

$$B_1(t) = (1-t)^2P_0 + 2(1-t)tP_1 + t^2P_2. \tag{3.8}$$

A few simulations and experiments were performed in [49]. The mean distance error of the cross join of the two sections was 1.7 mm. However, this approach has disadvantages because of the fact that each section is modelled by a quadratic Bézier curve. The Bézier curve is defined by three points: the starting point, the control point and the end point. This

makes that the quadratic Bézier can only model curves that lie in the same plane. Moreover, this method assumes that the rotations in one section are identical. When there are large payload, there would be the chance that the section transforms into S shape. Thus, the constant curvature assumption doesn't hold any more. Song *et al.* also reported from experiments that the proposed method is no longer valid when the angle of the curve is larger than $\frac{\pi}{2}$. To overcome these problems, S.Song *et al.* have improved their method in [50]. Each section of the continuum robot is now fitted by a cubic Bézier curve. Four points (the starting point, the end point and two control points) are needed to determined the cubic Bézier curve. By modeling each section as a cubic Bézier curve, the method is able to work if a section is deformed into different planes. Also by using higher order Bézier curves, the limitation of the total angle of the curve length is less restrictive. Allowable angles increase to π compared to the old method which limits the radian at $\frac{\pi}{2}$. Sadjadi *et al.* presented a method in [43] to improve the needle deflection estimation by fusing the position information of two EM sensors and the tip position estimated from a kinematic needle deflection model. The first EM sensor is installed on the needle base. Together with the needle deflection model, the needle tip postition can be estimated indirectly. A Kalman filter is then used to fuse the estimated tip position with the tip position measured from the second EM sensor attached on the needle tip. Dore *et al.* developed a catheter with multiple EM sensors placed along its length in [7]. A probabilistic framework is used to combine the spatial data provided by the EM sensors and the information from the catheter motion algorithm. This method allows continuously monitoring the shape and position of catheter within the lumen. Tran *et al.* introduced a new approach to reconstruct the 3D shape of the catheter by combining the discrete pose information of EM sensors and the 2D information extracted from fluoroscopic images [52]. This method was reported to give promising results which allow reconstructing the catheter shape with a median root-mean-square error of 3.7 mm with an interquartile range of 0.3 mm.

2 Discussion

EM tracking based shape reconstruction methods have several advantages such as easy to set up, freedom from light of sight restrictions and miniature-sized sensors. However, a major problem with EM tracking systems is that they are not able to provide uniform accuracy through out the tracking area. The desired highest accuracy is usually achieved in the center of the tracking volume. Another disadvantage of EM tracking systems is that they are highly susceptible to field distortion caused by electrically-conductive and magnetic materials [58]. Several compensation methods have been proposed to reduce the measurement errors of EM tracking systems, a summary can be found in [20]. Sadjadi *et al.* presented a method which combines a motion model with the information captured from redundant EM sensors to compensate for the field distortion in realtime [44]. EM tracking systems are widely used in the various application from different fields. However, futher investigations need to be made to bring EM tracking systems to the operating room in the ATLAS targeted disciplines.

4 Image based shape sensing

Shape sensing using FBGs [47, 24, 19, 42] and electromagnetic sensors [7, 49, 50] are quite common nowadays to find out the shape of surgical robotic manipulators. These techniques are efficient and show a lot of advantages like fast response time, miniaturisation, biocompatibility, non-toxic and high sensitive [18, 40, 42]. These techniques are fast and may be quite accurate, but, hardware modifications, non-transferable to other robots, integration with small and highly flexible robotic manipulators are quite challenging [25, 48]. Electromagnetic field distortions in EM tracking [18] and significant shape estimation error for highly deformable robots due to lower strain transfer efficiency onto Fiber Bragg Grating(FBG) sensor [48] also limit the successful implementation in shape sensing. On the other hand, image based shape sensing methods have the capability to measure the shape of robots without consuming extra space and requiring typically no major hardware modifications [38]. Image based technologies like fluoroscopy [32, 54, 15], endoscopy [37, 4] and ultrasound [5, 55] are quite popular to estimate the shape of robotic manipulators and catheter in minimally invasive surgery (MIS). However, these techniques have some disadvantages or challenges to be dealt with such as large radiation dose and dependence on nephrotoxic contrast agents in case of fluoroscopy, low resolution and signal-to-noise ratio of ultrasound images and obstructions in front of endoscopy cameras [48]. This chapter provides an overall state-of-the-art of the said image based shape sensing methods.

1 Fluoroscopy Based Shape Sensing

1.1 Introduction

Fluoroscopy is a medical imaging technique which uses ionising radiation to produce two dimensional images of the object. There are two kinds of fluoroscopy imaging process:

i monoplane fluoroscopy

ii biplane fluoroscopy

1.2 Monoplane Fluoroscopy

In monoplane fluoroscopy, an X-ray beam from an X-ray source is passed through the object and the transmitted ray from the object is captured by a screen or camera which is placed on the other side of the object. As shown in Fig.4.1, the C-arm consists of one X-ray source and a screen opposite to the source. In between these two, an object is placed. Unlike visible light, the X-ray can penetrate through most of the objects and produces images of the interior part of the object. The object absorbs different amounts of the X-ray beam depending upon it's density. This then leads to a certain contrast on the image captured by the detector or photographic film from which one may infer some anatomic structures or detect the location or shape of instruments.

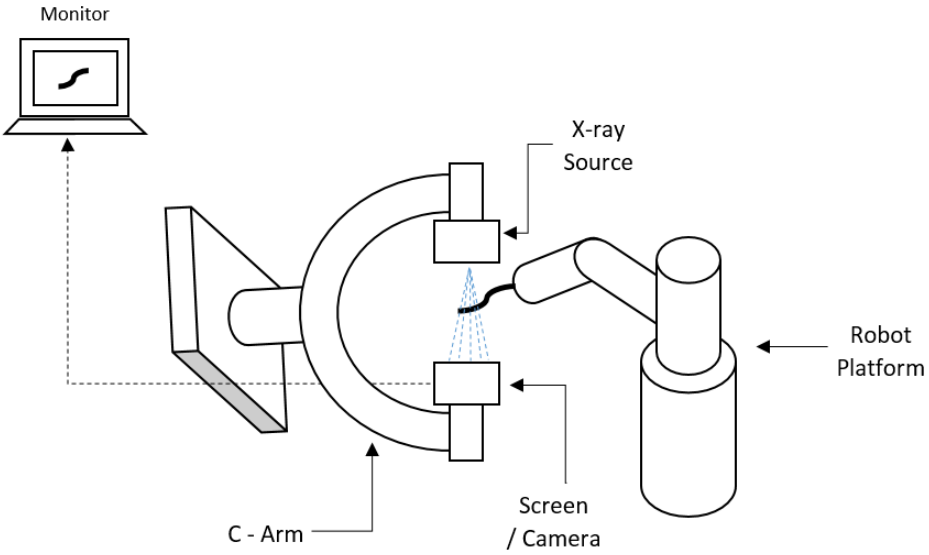

Figure 4.1: Monoplane Fluoroscopy Technique

1.3 Biplane Fluoroscopy

In the case of biplane fluoroscopy, two C-arms are placed independently around the object and images are acquired simultaneously. Each arm consists of an X-ray beam source and a detector/photographic film. This system simultaneously provides two views of the object at different positions using both the C-arms.

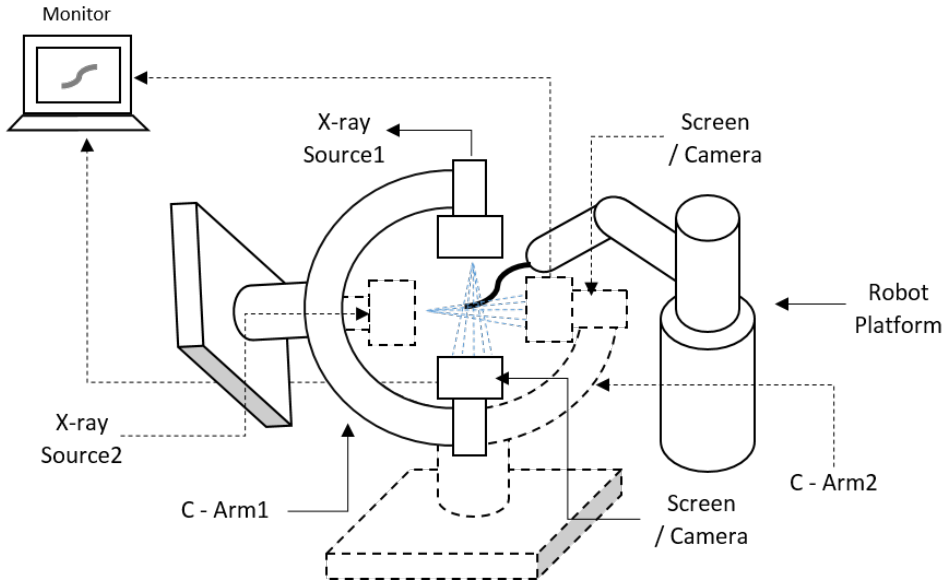

Figure 4.2: Biplane Fluoroscopy Technique

1.4 Methods and Description

The first step towards fluoroscopy shape sensing is to acquire images from mono- or biplane fluoroscopy. The fluoroscopy images are then processed using various segmentation algorithms [2, 45, 15] to find out the device centre line. A 3D reconstruction method using epipolar geometry [14] or based on kinematic modelling [32] can then be implemented to find the 3D shape of the device.

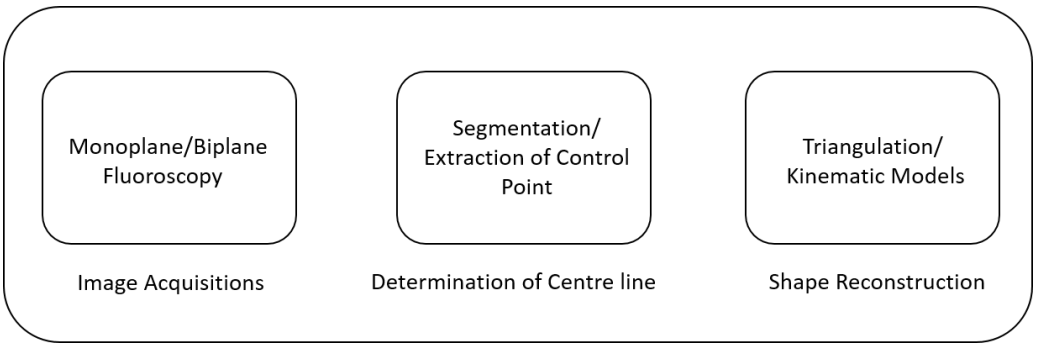

Figure 4.3: Fluoroscopy Based Shape Sensing Method

Baert *et al.* [2] used biplane fluoroscopy with epipolar geometry to reconstruct the 3D shape of a guidewire in the 3D vasculature. In this method a 2D tracking procedure is implemented based on energy minimization of spline parametrisation where the guidewire is tracked and presented as a third order B-spline line using acquired biplane images. Finally the epipolar geometry is used to reconstruct the 3D shape of the guidewire from the 2D biplane images using calibrated C-arm.

Schenderlein *et al.* [45] proposed an algorithm which implements the B-snake [26] algorithm with biplane fluoroscopy images to reconstruct the 3D shape of a catheter. A line enhancing feature image is calculated and utilised to generate 3D image forces from the 2D projections obtained from the biplane image system. To reconstruct the 3D pose of the catheter, missing image information caused by the asynchronous image acquisition is approximated by linear force interpolation using two consecutive images recorded by one of the C-arms. The evaluation of this algorithm is implemented on 33 virtual image datasets and the mean catheter pose error is found as 1.26 mm.

Hoffmann *et al.* [15] proposed a new method for reconstructing the 3D shape of a catheter using biplane fluoroscopy. In this approach, the 2D detection of the catheter is performed using three processes in which the parts of the catheter are identified based on image preprocessing. Then these are transformed into a graph to find an analytical representation model using the Dijkstra algorithm. In the last process, a final estimation of the 2D spline catheter is done using a graph search method. The catheter is then reconstructed into a 3D shape from the two 2D splines generated during the biplane fluoroscopy. Here the epipolar geometry is used. The method is evaluated using 66 biplane images of a catheter. As there are no 3D data available, the 3D reconstruction is forward projected into planes. The mean error is calculated as 0.7 mm$\pm$2.0 mm for the catheter. The error in 3D is calculated by acquiring 13 biplane images at different angulations [14]. The error of the robot shape is estimated as 1.2 mm$\pm$1.2 mm for circumferential mapping catheter and 1.3mm$\pm$1.0mm for the ablation catheter. This method is further extended [13] by implementing a learning based framework to adapt the arbitrary line shaped catheter used in Electrophysiology procedure. This approach can be adapted to catheters that undergo larger deformations such as coronary sinus catheters. The improved reconstruction error is measured as 1.8 mm$\pm$1.1 mm and 2.2 mm$\pm$2.2 mm on phantom and clinical data respectively.

Shape sensing methods using biplane fluoroscopy can be quite precise and consistent because biplane fluroscopy gives simultaneous views at various position of the instruments to find out their shape. However high ionising radiation dose, expensive and bulky instruments [48] limit the application during shape sensing. To solve these problems recent advancements of shape sensing is based on monoplane fluoroscopy. Otaka *et al.* [31] proposed a monoplane fluoroscopy based shape sensing solution to generate 3D shape of snakelike manipulators used in hip osteolysis. The proposed approach uses a piecewize intensity based 2D/3D registration from an X-ray projection with prior knowledge of shape and kinematic properties of the manipulator (for e.g. each rigid structure connected by a pin joint parameterized by a low degree polynomial basis) for pose estimation. The feasibility of this method is tested using simulated projection images of phantom of cadaveric system and femoral hip implants simulating a scenario of treating osteolytic regions during a hip revision surgery. The mean translation error of the base is found as 0.02 mm and 0.03 mm in x and y axes respectively while the joint angle error is estimated as less than 0.07 degree.

Papalazarou *et al.* [32] presented a non rigid structure from motion (NRSfM)) method with a robot kinematic model which uses monoplane X-ray projection made with a small view separation for reconstructing the 3D shape of a deforming curvilinear catheter. The combination of NRSfM and a kinematic model provides a low dimensional parametrization of the catheter which is then used with an X-ray imaging system to retrieve the 3D shape of the catheter. The suitability of this model is tested by moving the catheter in free space as well as inside a heart phantom model.

Vandini *et al.* [54] used an algorithm that fuses information acquired from monoplane X-ray images with a kinematic

model to estimate the real time shape of the continuum robot. The intra-operative tracking of the continuum robot from an X-ray projection is combined with a kinematic model of the robot using 2D/3D non rigid registration to find out the realtime shape. The algorithm does not require repositioning of the C-arm, thus making it suitable for use in a space constrained workplace. The proposed method of shape sensing estimates 0.88 mm as shape reconstruction error and 2.22 mm as tip tracking error.

The shape sensing methods described above are highly accurate and robust. However, these methods mostly rely on continuous exposure to ionising radiation, which produces 2% of cancers due to the excess use of these imaging technique [3]. To address this problem, Lobaton *et al.* [25] proposed a new idea which uses a small finite number of X-ray projection images to reconstruct the 3D shape of the robot. This approach first estimates the robot's shape using a kinematic model and then refines the shape using data acquired from monoplane X-ray projected images. To acquire the latter a method for optimal placement of C-arm which extracts images at discrete time points is derived. Although the method acquires discrete images at a certain point, it is capable of finding acceptable realtime shape estimates over the total procedure by integrating the previously extracted images with kinematics modelling. The method is implemented in a simulated bronchoscopy environment. A tip tracking error is estimated to be 0.8 mm.

As ATLAS mostly focuses on smart flexible robots which can autonomously propel through complex deformable tubular structure, shape sensing is essential to accurately control the robot without damaging the environment. In this case, Electromagnetic (EM) shape sensing may fail in the presence of other electrical components and FBG based shape sensing methods may not be implemented due to highly complex deformable structure of the robot [48]. As fluoroscopy techniques are free from electromagnetic interferences and calculation of strains, this technique should not be fully discarded and reemains a promising method for estimating the shape of these highly deformable robots accurately. Despite of these advantages of fluoroscopy imaging technology, limitations like the use of bulky and costly instruments and larger ionising radiation dosage remain a concern. Methods whereby different sensing modalities are fused could provide the best of both worlds while reducing the total radiation exposure. Further research should be done to use this technique safely in ATLAS targets.

2 Endoscopy Based Shape Estimation

2.1 Introduction

Despite extensive studies and research on fluoroscopy-based shape reconstruction, nearly all these methods suffer from high computational expenses, large radiation dosages and large cost [48]. Unlike fluoroscopy imaging, endoscopy based shape-reconstruction uses the images of the shape and distal tip pose of the instrument from an endoscopic camera to reconstruct the shape of the instrument. For this technology a direct line of sight is needed and use in an environment filled with blood is thus not an option. In the following an overview is given of reconstruction techniques based on this modality.

2.2 Methods and Discussion

The shape reconstruction procedure using endoscopes follows typically two approaches: i.e. marker-based and marker-less. In marker-based approaches, markers are placed on the instrument. The images from the endoscopic camera are forwarded to marker tracking algorithms that try to find out the position vector U_o of the instrument (observation). The estimated position vector U is calculated from the 3D screen rendering. The error e is then calculated between observations and estimated positions. The error is then fed to the visual servo control loop to find the state q of the instrument.

In case of marker-less approaches, for a given current state q, a feature point vector U_o (observations) is extracted by using a computer vision algorithm. The estimated positions vector U is calculated using a kinematic and a camera model. The error between observations and estimated positions is computed and fed to the control algorithm to reach accurate state estimates of the instrument. Reilink *et al.* [37] proposed a marker-less approach to reconstruct the 3D pose of a flexible endoscope. The images from the endoscopic camera are processed to find the feature points on the instruments. These features are compared with the calculated position of these points acquired from the kinematic model. Depending on the deviation between the model and observations, the constructed state of the model is updated repeatedly so as to match the model with observations. Reilink *et al.* [36] also presented marker-based approaches by placing four markers on the instrument. In this approach instead of feature points, the position information from the four markers is used to update the instrument's kinematic model. The approaches are tested inside a colon model. The marker-based approach, [35], produces RMS errors of tip tracking as small as 1.1 mm, 1.7 mm and 1.7 mm while the marker-less approach [35]

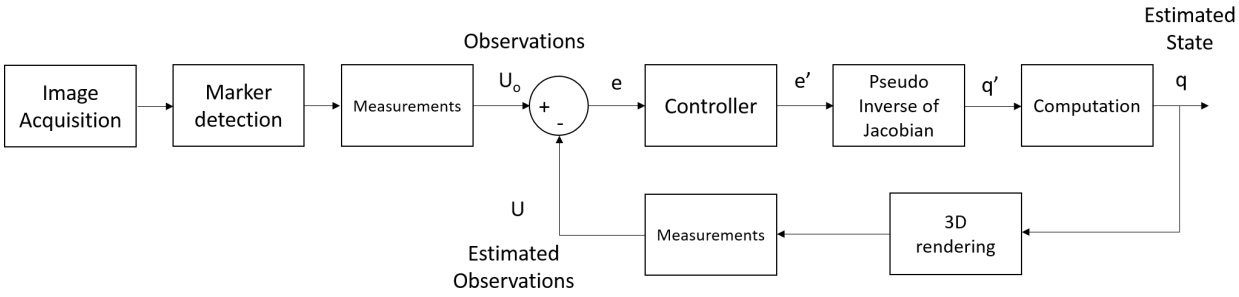

Figure 4.4: Marker-Based Shape Sensing Approach using Endoscopic Image

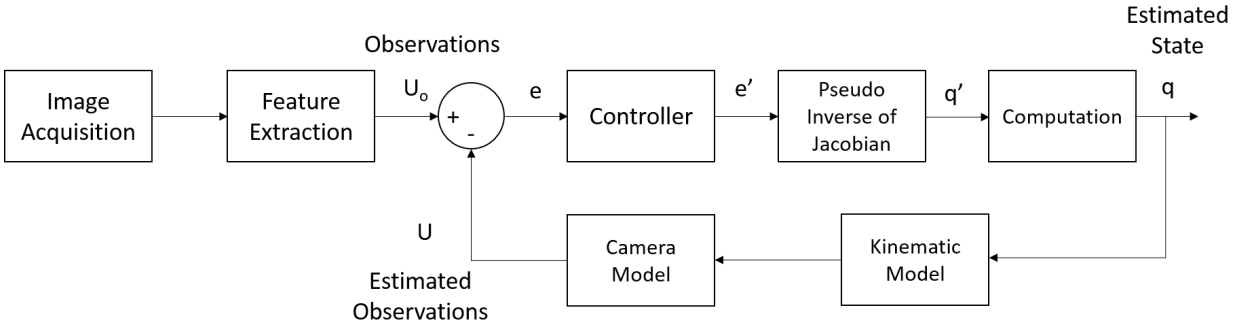

Figure 4.5: Marker-Less Shape Sensing Approach using Endoscopic Image

produces an RMS error of 1.5 mm, 1.6 mm and 1.8 mm in the X (horizontal), Y(vertical) and Z(away from the camera) direction respectively.

Both these methods require precise geometry and kinematic models of the robot. However, obtaining such precise geometry is very difficult and sometimes these methods don't produce good accuracy due to uncertainty in the model parameters [4]. Cabras *et al.* [4] presented an improved marker-based approach using supervised learning to reduce the uncertainty produced by previous models. With the support of coloured markers fixed to the instruments, this method uses an image segmentation stage followed by a stage for position estimation. In the beginning, the markers are segmented using an Adaptive Boosting algorithm trained by manually determining foreground and background samples from in vivo images taken during operations. Thereafter, the centroid of the markers are calculated and are used as input to the data pose estimation stage.

With disposable chip-on-tip cameras becoming available, endoscopy-based shape sensing methods could be implemented in ATLAS to avoid bulky and costly instruments. This technique uses the robot cameras to estimate the shape, thus eliminating the use of any external instrument and high radiation dosage. As this technique is successfully used for highly deformable continuum robots, it can be implemented in ATLAS targets to estimate the shape of the robot accurately. This can also reduce the space of workplace by eliminating lager size instruments which could be a great advantage in ATLAS where we aim to optimise the reachable workspace. However, a direct line of sight is required in this process to estimate the shape of the robot. Obstructions or occlusioins in this process will create problems in shape estimation. Further advancement in this research is important to implement this concept, possibly requiring fusion with other sensor modalities.

3 Ultrasound imaging Based Shape Estimation

Endoscope based imaging is able to estimate the shape of flexible instruments and robots in minimally invasive surgery pretty accurate without requiring any extra sensors in the robot. However the line of sight of the endoscopic camera creates a limitation for effective shape sensing of the flexible robots. Another fairly low-cost imaging modality which can be used to see through tissue and (some) obstacles is ultrasound. This sensing modality is surveyed in this section.

3.1 Introduction

Shape sensing based on ultrasound is an another alternative of medical imaging technology to estimate the shape and track the instruments without exposure to large radiation dosages. In spite of the fact that the images produced in ultrasound lack good visibility [6], this process could be used to estimate the shape consistently. In addition to this, ultrasound imaging is safe, fast, portable and economical. This imaging method has been implemented to detect the position of medical instruments [30, 29], to determine the position and orientation of long, thin surgical tools [53], to estimate needle deflection [56] or track the tips of steerable needles [57, 59] and to detect continuum curved robot [39, 38] in different minimally invasive surgery procedures. Moreover, this technique has also been implemented to reconstruct the shape of instruments and robots used in MIS procedures.

3.2 Methods and Discussion

Greer *et al.* [10] presented a real time segmentation method to reconstruct the 3D shape of curved needles using combined B-mode and power Doppler images from a tracked 2D ultrasound transducer. The approach consists of two steps - image analysis and curve fitting. The image analysis is implemented on pairs of power Doppler and B-node images. An external coil produces mechanical vibration which creates a Doppler response along the needle. This Doppler response is then processed in order to identify the region of interest in the B-mode ultrasound image. B-mode image analysis is performed within the region of interest to create a segmentation of the needle cross-section. Each section is processed to generate 2D candidate points for the reconstruction process. The 2D points are then transformed to 3D world coordinates by taking into account the ultrasound transducer pose. Finally, the 3D shape is reconstructed using these points with a curve fitting model. For comparison a reference manual segmentation is conducted by identifying the needle in each image manually and fitting a 3D polynomial to the identified points. The difference between the proposed segmentation method and the manual segmentation is 0.38 mm± 0.27 mm. The tip position differed 0.71 mm± 0.55 mm from the manually indicated tip position.

Carriere *et al.* [5] proposed a real time method to estimate the shape of a flexible needle by combining a kinematic bicycle model with axial Transrectal Ultrasound (TRUS) image segmentation. In this method, the location of the needle's cross section is segmented out of each of the image slices captured normal to the insertion direction of the needle using ultrasound imaging technology. The tracked cross section and the distance between successive image slices is incorporated by a particle filter to update the parameters of the kinematic model for each image slice. This approach is followed to predict the shape of the needle after complete insertion. The method is tested in ex-vivo beef phantom tissue and in-vivo clinical images and produces an average tip prediction error of 0.497 mm± 0.38 mm and 0.44 mm ± 0.15 mm respectively. Waine et al.[55] also employed 2D transverse ultrasound images to visualise 3D shape of the needle used in brachytherapy process. They applied an intensity thresholding approach to find out the potential locations of the needle within each 2D transverse ultrasound image. A Random Sample and Consensus (RANSAC) algorithm is then implemented to filter out the outliers and then remaining points are fitted in a polynomial model to reconstruct the 3D shape of the needle. The method is validated using 21 sets of ultrasound images of the brachytherapy needle embedded within a tissue phantom and the estimated shape of the needle differs 0.5mm with respect to shape measure using camera.

Shape sensing using 3D ultrasound imaging has also received much attention in MIS. Neshat *et al.* [28] proposed a novel method to detect the needle in real time using 3D ultrasound images. They presented an algorithm based on parameterization of the shape of the instrument (needle) using Bézier polynomials and the generalized Radon/Hough transform for real time detection of needle. This algorithm is implemented on a graphics processing units (GPU) using Compute Unified Device Architecture (CUDA) programming. The effectiveness of the method is tested in an experimental test-bed for robot-assisted image-guided minimally invasive lung brachytherapy and this approach is able to detect the tip and the axis of the needle axis accurately. Ren and Dupont [39, 38] introduced a new method to detect the the curved robot using 3D ultrasound imaging technique. This method fuses geodesic active contours and a speed function based on enhancement of tubularity of the robot for detecting curved continuum robot. The proposed method is tested in ex vivo intracardiac experiments. Although shape sensing using 3D ultrasound imaging is fast and accurate, the cost of 3D ultrasound systems as compared to 2D ultrasound devices are higher which limits the successful implementation of this 3D ultrasound method [55].

Fluoroscopy imaging method generally uses high radiation dosage and limits the application due to safety issues. Endoscopy based shape sensing needs a direct line of sight to perform shape sensing action. Ultrasound imaging can be an alternative to fluoroscopy shape sensing and endoscopy-based shape sensing to estimate the shape of robot without exposure to ionizing radiation. This method is safe and free from line of sight. This method is generally used for sensing the shape of needle used in MIS intervention. But this can also be used for estimating the shape of continuum robot accurately[39, 38]. As ATLAS deals mostly with continuum deformable robots, this method can be implemented for shape

sensing of robots. While this method shows a lot of advantages, low resolution and signal to noise ratio are challenges of ultrasound based shape sensing. Further research in this field is crucial for adopting this technology in applications targeted by ATLAS.

Table 4.1: Image Based Shape Sensing Models - slide 1

Authors	Imaging Principle	Methods	Tested Environment	Results
Baert *et al.*[2]	Biplane Fluoroscopy	2D tracking procedure based on on energy minimization of spline parametrisation with epipolar geometry	Intracranial anthropomorphic vascular phantom	Eroor not reported
Schenderlein *et al.* [45]	Biplane Fluroscopy	B-snake algorithm with Epipolar geometry	33 virtual images from patient data sets	Catheter pose error is 1.26mm and mean tip deviation is 3.28 mm
Hoffmann *et al.* [15]	Biplane Fluoroscopy	Graph search method with epipolar geometry	Clinical data	Mean error of robot shape is 0.7mm±2.0mm
Hoffmann *et al.* [14]	Biplane Fluoroscopy	Graph search method with epipolar geometry	Clinical and phantom data from cardiac intervention	Mean error of robot shape is 1.2mm±1.2mm for circumferential mapping catheter and 1.3mm±1.0mm for the ablation catheter
Hoffmann *et al.* [13]	Biplane Fluoroscopy	Graph search method with learning-based framework using epipolar geometry	Clinical and phantom data from cardiac intervention	Reconstruction error of 1.8mm±1.1mm on phantom data and 2.2mm±2.2mm on clinical data
Otaka *et al.* [31]	Monoplane Fluoroscopy	Piecewize intensity based 2D/3D registration with prior knowledge of shape and kinematic property	Snake-like robotic robot for hip osteolysis treatment	Mean translation error of base is found as 0.02mm and 0.03mm in x and y axes and the joint angle error is 0.07 degree

Table 4.2: Image Based Shape Sensing Models - slide 2

Authors	Imaging Principle	Methods	Tested Environment	Results
Papalazarou *et al.* [32]	Monoplane Fluoroscopy	Non rigid structure from motion(NRSfM)) method with a robot kinematic model	Moving the catheter in free space as well as inside a heart phantom model	Error not reported
Vandini et al.[54]	Monoplane Fluoroscopy	Intra-operative tracking kinematic model of the robot using 2D/3D non rigid registration	A skull phantoml	0.88mm as shape reconstruction error and 2.22mm as tip tracking error
Lobaton *et al.* [25]	Monoplane Fluoroscopy	Kinematic models with image data from optimal placed C-arm	A simulated lung phantom in bronchoscopy environment	The tip tracking error is 0.8mm
Reilink *et al.* [37]	Endoscopy Imaging	Marker-less method which uses feature points information to update the kinematic mode	A Colon phantom in transluminal endoscopic surgery	RMS values for tip tracking error are 1.1mm, 1.7mm, and 1.5 mm for three directions
Reilink *et al.* [36]	Endoscopy Imaging	Marker-based : position information from marker used with kinematic model	Colon phantom in transluminal endoscopic surgery	RMS values for tip tracking error are 1.1mm, 1.7mm, and 1.5mm for three directions

Table 4.3: Image Based Shape Sensing Models - slide 3

Authors	Imaging Principle	Methods	Tested Environment	Results
Cabras *et al.* [4]	Endoscopy Imaging	Marker-based approach using supervised learning	In vivo images	Robot shape error not available
Greer *et al.* [10]	2D Ultrasound Imaging	Using combined B-mode and power Doppler images	Nitinol needle inserted along a curved path in ex vivo bovine liver tissue	Shape segmentation error 0.38mm±0.27mm
Carriere *et al.* [5]	2D Ultrasound Imaging	Combining a kinematic bicycle model with axial Transrectal Ultrasound (TRUS)image segmentation	Ex-vivo beef phantom tissue and in-vivo clinical images	Tip prediction error of 0.497±0.38mm for ex-vivo beef phantom tissue and 0.44±0.15mm for in-vivo clinical images
Waine *et al.* [55]	2D Ultrasound Imaging	Intensity thresholding approach with Random Sample and Consensus (RANSAC) algorithm	Brachytherapy needle embedded within a tissue phantom	Shape estimation error 0.5mm
Neshat *et al.* [28]	3D Ultrasound Imaging	Bézier polynomials with generalized Radon/Hough transform	In an experimental test-bed for robot-assisted image-guided minimally invasive lung brachytherapy	Mean axis error for different needles: 0.48mm for 18 gauge brachytherapy, 0.57mm for 22 gauge brachytherapy and 1.06 for pre-bent needles into a gelatin agar cube

5 Electrical Impedance Tomography (EIT) and Resistance Based Shape Estimation

1 Introduction

Shape sensing using electromagnetic tracking methods, imaging techniques and optical methods can be quiet efficient and accurate [50, 54, 42]. However, these techniques have some limitations. Electromagnetic tracking methods are affected by the presence of other magnetic or ferromagnetic materials or fields, making their use difficult in the environments where other instruments or coils are present [**franz2014electromagnetic**]. Low resolution, high radiation dosages and the use of bulky instruments [48] in the case of different imaging methods create challenges for potential applications in shape sensing. FBG shape sensors may exhibit significant shape estimation errors in highly deformable structures [48] and while having low diameters they do require space for integration.

Electrical impedance tomography (EIT) and resistance based shape sensing methods have been received much attention nowadays with the hope to solve at least some of the abovementioned problems for shape sensing. EIT and resistance based shape sensing work by attaching several sensors on the robot body. Where, EIT applies a current through surface electrodes and measures electrical voltage to reconstruct the conductivity distribution and to obtain the tomographic image of the interior structure of the object [**boyle2012shape**], in the case of resistive based shape sensing, current is sent through a sensor to measure the change in resistance of the sensor. This change is used to find the shape and tip position of the robots [**gerboni2017feedback**]. Although EIT and resistance based shape sensing come with some advantages, the wiring of the different sensors remains a challenge for implementing these methods. An overview of both type of sensing methods is explained in the following.

2 EIT Based Shape Sensing Method

2.1 Method and Discussion

For EIT typically, several conducting surface electrodes are attached to the boundary of the conductive object that is being inspected. In each step, two electrodes are selected and an electrical current is applied through these electrodes. The other electrodes are used to measure the electrical potential which is produced at the boundary of the object (see Fig.5.1) [**avery2019shape**, **visentin2018flexible**]. The electrodes used for injecting electric current are referred to as *driving* electrodes, while the other electrodes used for electrical potential measurement are referred to as *measurement* electrodes. The distribution of current inside the object varies according to the local variations in internal permittivity or conductivity which results in changes of electrical potential at the boundary of the object. This process is repeated for each electrode pair until a full cycle is accomplished. Finally, an approximated resistivity distribution inside the object is estimated by implementing an image reconstruction algorithm.

Using this concept Avery *et al.* [**avery2019shape**] presented a novel method to estimate the shape of a variable stiffness soft robot. A new frequency division method (FDM) EIT concept is implemented in which multiple currents at different frequencies were injected through different electrode pairs simultaneously. The commonly used EIT limits the temporal resolution of the impedance images due to switching of injection electrodes. The FDM-based EIT method decreases the data acquisition time by removing the need for switching injection electrode pairs. This in turn increases the temporal resolution of the impedance images [**dowrick2018phase**]. This method is tested both in a hydraulic hinged actuator and a pneumatic finger actuator with hydraulic beams using saline as a working fluid. The saline solution acts as both actuation fluid and as a conductive medium for EIT measurements. A parallel system with six independent current sources that can inject current at different frequencies is used in this method to apply current to electrode pairs and a DAQ system is used to measure the electrical potentials across the electrodes. Then conductivity changes are reconstructed from measured electrical potentials using quasi-static Maxwell equations with electrode model boundary conditions for one pair of electrodes. Finally, the EIT image reconstruction is performed by employing a dedicated method [**aristovich2014method**] to find the shape of the robot.

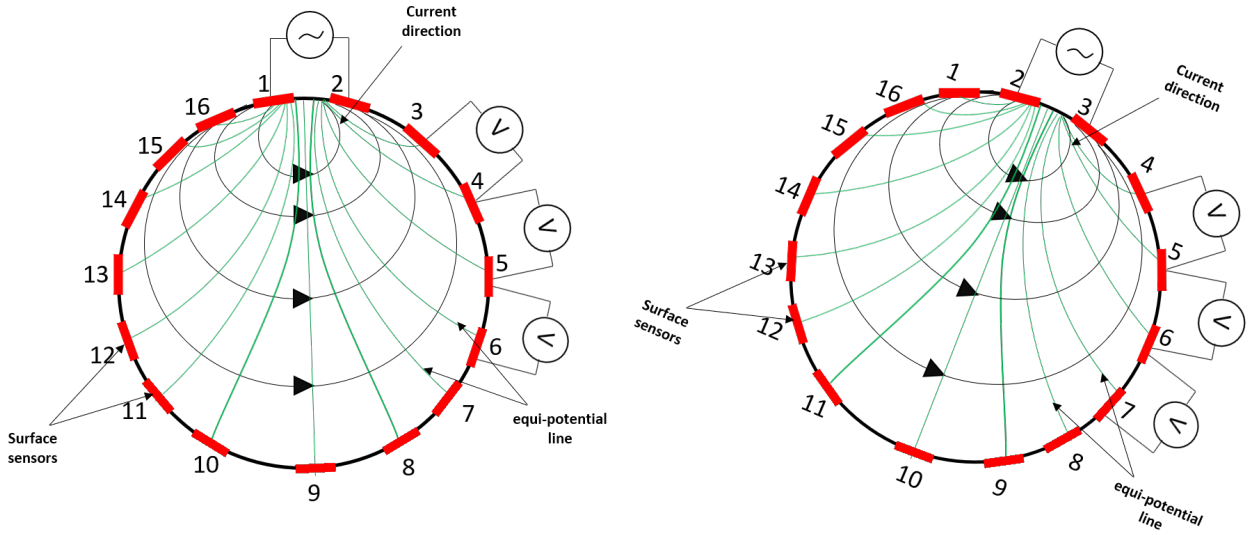

Figure 5.1: Overview of EIT technique. Electrical current is injected into two electrodes, while other electrodes are used to measure the electrical potential produced between them at the boundary. The current injection and measurement process is repeated by changing driving electrodes until a full cycle is accomplished. In the figure, red lines indicate surface electrodes, black lines show the field lines following the current direction and green lines are equipotential lines.

3 Resistance Based Shape Sensing Method

3.1 Methods and Discussion

In case of resistance based shape sensing, several strain sensors are attached on the body of a flexible robot. The resistance of these sensors changes when there is a longitudinal and bending strain across the sensor. The change in resistance is then processed and used with some mechanical model [**renda2012general**] to reconstruct the shape of the robot [**renda2012general**].

Cianchetti *et al.* [**cianchetti2012sensorization**] presented a novel method which uses stretch sensors to reconstruct the spatial configuration of a continuum soft robot. In this method 20 pieces of conductive textile material are placed on two sides of an octopus-inspired arm prototype which is made up of silicon. The conductive textile produces change in resistance when the shape of the robot changes. Using this information, the relation between strain and resistance is estimated. Then a spatial configuration reconstruction method given by Renda *et al.* [**renda2012general**] is implemented to reconstruct the shape of the robot.

Wurdemann *et al.* [**wurdemann2015embedded**] proposed a shape sensing solution using conductive yarn to estimate the shape of the soft manipulator. Three pieces of conductive yarn have been embedded inside a soft manipulator made from silicon with three pneumatic actuation chambers. When an elongation in the conductive yarn takes place, the yarn material shrinks laterally producing a change in electrical resistance of yarn. The relation between the length and electrical resistance of yarn can be determined and further used to calculate the bending curvature, bending angle and orientation of the soft manipulator.

The EIT and resistance-based shape sensing methods are free from electromagnetic interference and high radiation dosage. Overall the cost of this technology is low, but integration and wiring remains a challenge. Further exploration in this field would be needed before implementation of this method in ATLAS.

Bibliography

[1] Richard Askey. “The 1839 paper on permutations: its relation to the Rodrigues formula and further developments”. In: *Mathematics and Social Utopias in France: Olinde Rodrigues and His Times. Edited by Simon Altmann and Eduardo. L. Ortiz. History and Mathematics* 28 (2005), pp. 105–18.

[2] Shirley AM Baert et al. “Three-dimensional guide-wire reconstruction from biplane image sequences for integrated display in 3-D vasculature”. In: *IEEE transactions on medical imaging* 22.10 (2003), pp. 1252–1258.

[3] David J Brenner and Eric J Hall. “Computed tomography-an increasing source of radiation exposure”. In: *New England Journal of Medicine* 357.22 (2007), pp. 2277–2284.

[4] Paolo Cabras et al. “Comparison of methods for estimating the position of actuated instruments in flexible endoscopic surgery”. In: *2014 IEEE/RSJ International Conference on Intelligent Robots and Systems*. IEEE. 2014, pp. 3522–3528.

[5] Jay Carriere et al. “Real-time needle shape prediction in soft-tissue based on image segmentation and particle filtering”. In: *2016 IEEE International Conference on Advanced Intelligent Mechatronics (AIM)*. IEEE. 2016, pp. 1204–1209.

[6] Stephanie Cheung and Robert Rohling. “Enhancement of needle visibility in ultrasound-guided percutaneous procedures”. In: *Ultrasound in medicine & biology* 30.5 (2004), pp. 617–624.

[7] Alessio Dore et al. “Catheter navigation based on probabilistic fusion of electromagnetic tracking and physically-based simulation”. In: *2012 IEEE/RSJ International Conference on Intelligent Robots and Systems*. IEEE. 2012, pp. 3806–3811.

[8] Alfred M Franz et al. “Electromagnetic tracking in medicine - a review of technology, validation, and applications”. In: *IEEE transactions on medical imaging* 33.8 (2014), pp. 1702–1725.

[9] James M Gere and S Timoshenko. “Mechanics of materials Brooks”. In: *Cole, Pacific Grove, CA* (2001), pp. 815–39.

[10] Joseph D Greer et al. “Real-time 3D curved needle segmentation using combined B-mode and power Doppler ultrasound”. In: *International Conference on Medical Image Computing and Computer-Assisted Intervention*. Springer. 2014, pp. 381–388.

[11] Kirsten R Henken et al. “Error analysis of FBG-based shape sensors for medical needle tracking”. In: *IEEE/ASME Transactions on mechatronics* 19.5 (2013), pp. 1523–1531.

[12] Kenneth O Hill and Gerald Meltz. “Fiber Bragg grating technology fundamentals and overview”. In: *Journal of lightwave technology* 15.8 (1997), pp. 1263–1276.

[13] Matthias Hoffmann et al. “Electrophysiology catheter detection and reconstruction from two views in fluoroscopic images”. In: *IEEE transactions on medical imaging* 35.2 (2015), pp. 567–579.

[14] Matthias Hoffmann et al. “Reconstruction method for curvilinear structures from two views”. In: *Medical Imaging 2013: Image-Guided Procedures, Robotic Interventions, and Modeling*. Vol. 8671. International Society for Optics and Photonics. 2013, 86712F.

[15] Matthias Hoffmann et al. “Semi-automatic catheter reconstruction from two views”. In: *International Conference on Medical Image Computing and Computer-Assisted Intervention*. Springer. 2012, pp. 584–591.

[16] Sonja Jäckle, Jan Strehlow, and Stefan Heldmann. “Shape Sensing with Fiber Bragg Grating Sensors”. In: *Bildverarbeitung für die Medizin 2019*. Springer, 2019, pp. 258–263.

[17] Sonja Jäckle et al. “Fiber optical shape sensing of flexible instruments for endovascular navigation”. In: *International journal of computer assisted radiology and surgery* (2019), pp. 1–9.

[18] Beobkyoon Kim et al. “Optimizing curvature sensor placement for fast, accurate shape sensing of continuum robots”. In: *2014 IEEE international conference on robotics and automation (ICRA)*. IEEE. 2014, pp. 5374–5379.

[19] Jin Seob Kim et al. “Shape determination during needle insertion with curvature measurements”. In: *2017 IEEE/RSJ International Conference on Intelligent Robots and Systems (IROS)*. IEEE. 2017, pp. 201–208.

[20] Volodymyr V Kindratenko. "A survey of electromagnetic position tracker calibration techniques". In: *Virtual Reality* 5.3 (2000), pp. 169–182.

[21] Sungyeop Lim and Soonhung Han. "A formula for the arc length of a superhelix". In: *Sensors and Smart Structures Technologies for Civil, Mechanical, and Aerospace Systems 2016*. Vol. 9803. International Society for Optics and Photonics. 2016, p. 980327.

[22] Sungyeop Lim and Soonhung Han. "Helical extension method for solving the natural equation of a space curve". In: *Surface Topography: Metrology and Properties* 5.3 (2017), p. 035002.

[23] Sungyeop Lim and Soonhung Han. "Shape estimation of a bent and twisted cylinder using strain from a sensor array in triple helices". In: *Measurement Science and Technology* 29.9 (2018), p. 095003.

[24] Hao Liu et al. "Large deflection shape sensing of a continuum manipulator for minimally-invasive surgery". In: *2015 IEEE International Conference on Robotics and Automation (ICRA)*. IEEE. 2015, pp. 201–206.

[25] Edgar J Lobaton et al. "Continuous shape estimation of continuum robots using X-ray images". In: *2013 IEEE International Conference on Robotics and Automation*. IEEE. 2013, pp. 725–732.

[26] Sylvie Menet. "B-snakes: Implementation and application to stereo". In: *Proceedings of Third International Conference on Computer Vision, 1990*. 1990.

[27] Jason P Moore and Matthew D Rogge. "Shape sensing using multi-core fiber optic cable and parametric curve solutions". In: *Optics express* 20.3 (2012), pp. 2967–2973.

[28] Hamid Reza Sadeghi Neshat and Rajni V Patel. "Real-time parametric curved needle segmentation in 3D ultrasound images". In: *2008 2nd IEEE RAS & EMBS International Conference on Biomedical Robotics and Biomechatronics*. IEEE. 2008, pp. 670–675.

[29] Paul M Novotny et al. "Gpu based real-time instrument tracking with three dimensional ultrasound". In: *International Conference on Medical Image Computing and Computer-Assisted Intervention*. Springer. 2006, pp. 58–65.

[30] Paul M Novotny et al. "GPU based real-time instrument tracking with three-dimensional ultrasound". In: *Medical image analysis* 11.5 (2007), pp. 458–464.

[31] Yoshito Otake et al. "Piecewise-rigid 2D-3D registration for pose estimation of snake-like manipulator using an intraoperative x-ray projection". In: *Medical Imaging 2014: Image-Guided Procedures, Robotic Interventions, and Modeling*. Vol. 9036. International Society for Optics and Photonics. 2014, 90360Q.

[32] Chrysi Papalazarou, Peter MJ Rongen, et al. "3D catheter reconstruction using non-rigid structure-from-motion and robotics modeling". In: *Medical Imaging 2012: Image-Guided Procedures, Robotic Interventions, and Modeling*. Vol. 8316. International Society for Optics and Photonics. 2012, p. 831620.

[33] Yong-Lae Park et al. "Real-time estimation of 3-D needle shape and deflection for MRI-guided interventions". In: *IEEE/ASME Transactions On Mechatronics* 15.6 (2010), pp. 906–915.

[34] Qiao Qiao et al. "Estimating and Localizing External Forces Applied on Flexible Instruments by Shape Sensing". In: *Proceedings 2019 IEEE Conference on Advanced Robotics*. Belo Horizonte, Brasil: IEEE, Dec. 2019.

[35] Rob Reilink, Stefano Stramigioli, and Sarthak Misra. "3D position estimation of flexible instruments: marker-less and marker-based methods". In: *International journal of computer assisted radiology and surgery* 8.3 (2013), pp. 407–417.

[36] Rob Reilink, Stefano Stramigioli, and Sarthak Misra. "Pose reconstruction of flexible instruments from endoscopic images using markers". In: *2012 IEEE International Conference on Robotics and Automation*. IEEE. 2012, pp. 2938–2943.

[37] Rob Reilink, Stefano Stramigioli, and Sarthak Misra. "Three-dimensional pose reconstruction of flexible instruments from endoscopic images". In: *2011 IEEE/RSJ International Conference on Intelligent Robots and Systems*. IEEE. 2011, pp. 2076–2082.

[38] Hongliang Ren and Pierre E Dupont. "Tubular enhanced geodesic active contours for continuum robot detection using 3d ultrasound". In: *2012 IEEE International Conference on Robotics and Automation*. IEEE. 2012, pp. 2907–2912.

[39] Hongliang Ren and Pierre E Dupont. "Tubular structure enhancement for surgical instrument detection in 3D ultrasound". In: *2011 Annual International Conference of the IEEE Engineering in Medicine and Biology Society*. IEEE. 2011, pp. 7203–7206.

[40] Roy J Roesthuis, Sander Janssen, and Sarthak Misra. "On using an array of fiber Bragg grating sensors for closed-loop control of flexible minimally invasive surgical instruments". In: *2013 IEEE/RSJ International Conference on Intelligent Robots and Systems*. IEEE. 2013, pp. 2545–2551.

[41] Roy J Roesthuis et al. "Three-dimensional needle shape reconstruction using an array of fiber bragg grating sensors". In: *IEEE/ASME transactions on mechatronics* 19.4 (2013), pp. 1115–1126.

[42] Seok Chang Ryu and Pierre E Dupont. "FBG-based shape sensing tubes for continuum robots". In: *2014 IEEE International Conference on Robotics and Automation (ICRA)*. IEEE. 2014, pp. 3531–3537.

[43] Hossein Sadjadi, Keyvan Hashtrudi-Zaad, and Gabor Fichtinger. "Fusion of electromagnetic trackers to improve needle deflection estimation: simulation study". In: *IEEE transactions on Biomedical Engineering* 60.10 (2013), pp. 2706–2715.

[44] Hossein Sadjadi, Keyvan Hashtrudi-Zaad, and Gabor Fichtinger. "Simultaneous electromagnetic tracking and calibration for dynamic field distortion compensation". In: *IEEE Transactions on Biomedical Engineering* 63.8 (2015), pp. 1771–1781.

[45] Marcel Schenderlein et al. "Catheter tracking in asynchronous biplane fluoroscopy images by 3D B-snakes". In: *Medical Imaging 2010: Visualization, Image-Guided Procedures, and Modeling*. Vol. 7625. International Society for Optics and Photonics. 2010, 76251U.

[46] Shahriar Sefati et al. "A highly sensitive fiber Bragg Grating shape sensor for continuum manipulators with large deflections". In: *2017 IEEE SENSORS*. IEEE. 2017, pp. 1–3.

[47] Shahriar Sefati et al. "FBG-Based Position Estimation of Highly Deformable Continuum Manipulators: Model-Dependent vs. Data-Driven Approaches". In: *2019 International Symposium on Medical Robotics (ISMR)*. IEEE. 2019, pp. 1–6.

[48] Chaoyang Shi et al. "Shape sensing techniques for continuum robots in minimally invasive surgery: A survey". In: *IEEE Transactions on Biomedical Engineering* 64.8 (2016), pp. 1665–1678.

[49] Shuang Song et al. "Real-time shape estimation for wire-driven flexible robots with multiple bending sections based on quadratic Bézier curves". In: *IEEE Sensors Journal* 15.11 (2015), pp. 6326–6334.

[50] Shuang Song et al. "Shape reconstruction for wire-driven flexible robots based on Bézier curve and electromagnetic positioning". In: *Mechatronics* 29 (2015), pp. 28–35.

[51] Daniele Tosi et al. "Fiber optic sensors for sub-centimeter spatially resolved measurements: Review and biomedical applications". In: *Optical Fiber Technology* 43 (2018), pp. 6–19.

[52] Phuong Toan Tran et al. "3D catheter shape reconstruction using electromagnetic and image sensors". In: *Journal of Medical Robotics Research* 2.03 (2017), p. 1740009.

[53] Marián Uherčık et al. "Model fitting using RANSAC for surgical tool localization in 3-D ultrasound images". In: *IEEE Transactions on Biomedical Engineering* 57.8 (2010), pp. 1907–1916.

[54] A. Vandini et al. "Vision-based intraoperative shape sensing of concentric tube robots". In: *2015 IEEE/RSJ International Conference on Intelligent Robots and Systems (IROS)*. Sept. 2015, pp. 2603–2610. DOI: 10.1109/IROS.2015.7353732.

[55] Michael Waine et al. "3d shape visualization of curved needles in tissue from 2d ultrasound images using ransac". In: *2015 IEEE International Conference on Robotics and Automation (ICRA)*. IEEE. 2015, pp. 4723–4728.

[56] Michael Waine et al. "Needle tracking and deflection prediction for robot-assisted needle insertion using 2d ultrasound images". In: *Journal of Medical Robotics Research* 1.01 (2016), p. 1640001.

[57] Zhouping Wei et al. "Oblique needle segmentation for 3D TRUS-guided robot-aided transperineal prostate brachytherapy". In: *2004 2nd IEEE International Symposium on Biomedical Imaging: Nano to Macro (IEEE Cat No. 04EX821)*. IEEE. 2004, pp. 960–963.

[58] Ziv Yaniv et al. "Electromagnetic tracking in the clinical environment". In: *Medical physics* 36.3 (2009), pp. 876–892.

[59] Yue Zhao, Hervé Liebgott, and Christian Cachard. "Tracking micro tool in a dynamic 3D ultrasound situation using Kalman filter and RANSAC algorithm". In: *2012 9th IEEE International Symposium on Biomedical Imaging (ISBI)*. IEEE. 2012, pp. 1076–1079.

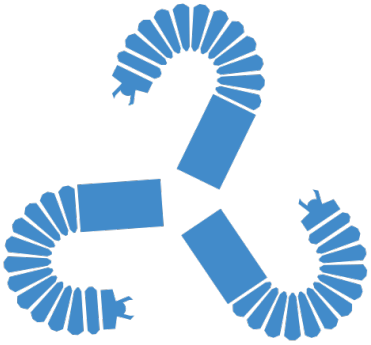

The ATLAS project

lastly modified: May 13, 2020

ATLAS-D2.2-1.0.1

Horizon 2020